The Characteristics of Late Summer Extreme Precipitation in Northern China and Associated Large-scale Circulations

Chen Zhiheng[1], Jie Zhang[1*]

1. Key Laboratory of Meteorological Disaster, Ministry of Education (KLME) /Joint International Research Laboratory of Climate and Environment Change (ILCEC)/ Collaborative Innovation Center on Forecast and Evaluation of Meteorological Disasters (CIC-FEMD), Nanjing University of Information Science & Technology, Nanjing, 210044, China

Corresponding author: Jie Zhang*, gs-zhangjie@163.com; Zhangj@nuist.edu.cn

This article has been accepted for publication and undergone full peer review but has not been through the copyediting, typesetting, pagination and proofreading process which may lead to differences between this version and the Version of Record. Please cite this article as doi: 10.1002/joc.6512

Abstract

Extreme precipitation occurs frequently in northern China. Understanding the characteristics of extreme precipitation is conducive to improving prediction accuracy rates of extreme precipitation events and disaster prevention. An analysis of 55-year daily precipitation data, which has been represented by R10mm since 1961, reveals non-uniform variations in late summer extreme precipitation in northern China. The study aims at establishing an objective classification of major impact large-scale circulations corresponding to extreme precipitation events. Utilizing the circulation classification, this study divides extreme precipitation events into the westerly mode (WM), westerly subtropical mode (WSM) and typhoon mode (TYM), thereby carrying out individual evaluations of types of extreme precipitation in northern China. The results indicate that the frequency distributions of WM and WSM in northern China both have decadal characteristics. Highly frequent WM from the 1980s to the early 2000s is a response to the enhancement of meridionality in westerly winds, which could strengthen the latitudinal positive-negative-positive circulation distribution of Pacific-Japan wave train patterns in East Asia; however, the late summer WSM in northern China is different from WM. The enhancement (abatement) of the westerly wind meridionality and relatively southward (northward) position of the Western Pacific subtropical high (WPSH) leads to a stretching southward (northward) front rain belt on the northwest edge of WPSH, thereby favoring WSM in Central China and East China (North China, Northeast China and the eastern parts of Northwest China). The decadal variations in the meridionality in westerly winds and

WPSH positions are closely related to sea surface temperature anomalies in the North Atlantic and Pacific Decadal Oscillation (PDO), respectively. The results of this study provide theoretical references for decadal extreme precipitation predictions.

Keywords: extreme precipitation; large-scale circulations; westerly wind meridionality

1. Introduction

Devastating catastrophes such as floods, landslides, debris flows and so on have increasingly emerged in summertime as the result of extreme precipitation events and have threatened the security of people's lives and properties (Easterling et al., 2000; Greenough et al., 2001; Meehl and Tebaldi 2004; Negri et al. 2005; Du et al., 2013; Van den Besselaar et al., 2013; Song et al., 2015). Several flood disasters have occurred in China in the last two decades, especially the catastrophic flood in the Yangtze River Basin in 1998, which caused serious casualties and enormous property losses (Cheng et al. 2001). Therefore, the extreme precipitation events in China have become a heated topic of debate in the past few decades (Ning and Qian, 2009). With a southern flooding-northern drought pattern in China (Wang 2001; Yu et al. 2004), the frequency, severity, and duration of droughts in northern China have risen (Zhang et al., 2019), which has resulted in extreme precipitation events in northern China attracting relatively less attention than in southern China. However, the ecological environment and water storage in northern China is particularly vulnerable, especially in arid areas due to climate change (Wang et al., 2017). Moreover, extreme precipitation in northern China has already caused destructive impacts on society. For example, on July 21st, 2012, a record-breaking rainstorm (exceeding the 1951 disaster) struck Beijing in northern China, leading to the deaths of 79 people in Beijing and causing economic losses exceeding 2 billion U.S. dollars (Zhu and Xue 2016). Average precipitation reached 190 mm in 24 hours for the whole city, and precipitation amounts in individual areas even reached 460 mm. Thus, the problem of extreme precipitation in northern China needs to be explored, and this study calls for further follow-up on this topic.

Extreme precipitation relates closely to vapor conditions, dynamic conditions, and so on. Large-scale circulation systems have major impacts on local precipitation anomalies in synoptic-scale systems (Liu et al., 2015) via affecting water vapor convergence and ascending motions and, ultimately, by limiting extreme precipitation areas. Meanwhile, large-scale circulation systems move relatively slowly and maintain for a relatively long time, thus leading to prolonged extreme climate events; these events include the persistent precipitation over South China in June 2010, which is considered to be associated with large-scale circulation anomalies (Yuan et al., 2012). Thus, large-scale circulations may play a dominant role in the background fields of extreme precipitation events, and a relationship must be established between large-scale circulations and extreme precipitation in northern China.

On the climate scale, extratropical westerly systems, including the Ural blocking, blocking high over the Sea of Okhotsk, and so on, (Chen and Zhai, 2014a; Zhang et al., 2017) could affect related factors of extreme events in China, such as divergent circulations with ascending motions in extreme precipitation events (Yuan et al., 2012). From a wave perspective, extratropical westerly systems are the manifestation of quasi-stationary wave trains. Orsolini et al., (2015) pointed out that extreme precipitation events over northern China in August 2010 were associated with quasi-stationary wave trains propagating eastwards across Eurasia. Anomalous high-amplitude quasi-stationary Rossby waves are linked to extreme precipitation events as well. Petoukhov et al. (2016) suggested that the quasi-resonant amplification of planetary waves have occurred, and it is the quasi-resonant amplification mechanism in amplifying planetary waves that favored Northern Hemisphere weather extremes, such as the Indus river flood in Pakistan in 2010.

In addition to extratropical westerly anomalies, signals from subtropical zones cannot be neglected either. China is situated on the eastern coast of Asia, adjoining the Pacific Ocean. The prevailing East Asian summer monsoon (EASM) is the transporter of oceanic water vapor for summer precipitation in China and plays a key role in affecting extreme precipitation events (Li et al., 2017; Wang et al., 2016). As an irreplaceable component of EASM, the characteristics of WPSH, such as intensity, shape and location, not only regulate the large-scale circulations and summer climate in East Asia (Tao and Chen, 1987; Lu et al., 2016; Huang et al., 2015; Yang et al., 2017) but could also be the precursor for extreme precipitation (Chen and Zhai, 2015). In terms of water vapor conditions, WPSH impacts the paths of water vapor brought by EASM and determines the anomalous moisture convergence zone (Chen and Zhai, 2014b; Qian and Shi, 2017) that limits the extreme precipitation zones in China. In terms of dynamical and thermal conditions, when the WPSH extends relatively westward, the anomalous warm and moist southwest monsoon flow will land on China. With the cooperation of the warm and moist airflow and the cold airflow from the mid and high latitudes, an anomalous convergence and ascending motion occur, which contributes to the precipitation extremes in China (Zhou and Yu, 2005; Mao and Wu, 2006; Ren et al., 2013).

As mentioned above, westerly and subtropical anomalies could both explain the variability in extreme precipitation in northern China; however, a comprehensive consideration containing both kinds of large-scale circulation systems and their corresponding extreme precipitation in northern China is needed but, currently, has not been studied thoroughly. For understanding the association between large-scale circulations and the variability in near-surface climate, the circulation classification is a well-established approach for exploring the dynamics of major impact large-scale circulations (Chen 2000; Yarnal et al. 2001; Belleflamme et al. 2015). For extreme precipitation events, previous studies focused mostly on the synoptic characteristics of extreme precipitation events during a particular period. Circulation classification indicators that partition major impact synoptic systems corresponding to specific extreme precipitation events have been established (Sun et al., 2016). However, few studies address climatic variations in extreme precipitation in northern China over several decades. The classification of partitioning major impact large-scale circulations corresponding to extreme precipitation events remains incomplete. A thorough understanding of the problems stated in this paper may assist in reducing adverse effects from disasters via developing coping strategies and improving predictions of extreme precipitation events in northern China.

Extraneous forcing sources, such as surface thermal anomalies or sea surface temperature anomalies could affect the anomalies of large-scale atmospheric circulations (Bates et al., 2001) The North Atlantic Oscillation (NAO) in response to the North Atlantic tripole sea surface temperature (Peng et al., 2003) could modulate the anomalous large-scale atmospheric circulation systems (Li et al., 2008). Meanwhile, NAO and Atlantic Multidecadal Oscillation (AMO) were documented as major drivers for the variability in precipitation extremes over the monsoon region in China (Gao et al., 2017). Moreover, a sea surface temperature anomaly (SSTA) in the western Pacific warm pool can trigger the Pacific-Japan (PJ) pattern (Nitta, 1987). PJ pattern may connect with extreme precipitation in northern China with its influence on EASM (Kawamura et al., 1996) and on tropical cyclone activity, which have been proven to be responsible for precipitation extremes over the Korean peninsula (Kim et al., 2012). Currently, the main forcing sources of extreme precipitation in northern China have been lightly studied but must still be addressed and be more thoroughly understood.

The paper is organized as follows. The data and methods containing extreme precipitation classification indicators are introduced in Section 2. Sections 3 and 4 introduce the spatial-temporal distribution of extreme precipitation in northern China, the large-scale circulations affecting extreme precipitation in northern China and their forcing sources. In Section 5, a summary is provided.

2. Data and methods

2.1 Data

Diurnal observational precipitation data from 753 stations in China during July August from 1961 to 2015 are the main analysis content (the data from 1961 to 2010 were compiled by the National Climate Center and the data from 2011 to 2015 were compiled by the China Meteorological Data Network). In northern China, 408 observation stations were selected as the research objects, which are located above 30° N and have less than 10 years of missing observations.

The reanalysis datasets are the ERA40 daily data from 1961 to 1978 and the Interim (ERA-Interim) daily data from 1979 to 2015, both of which are from the European Center Medium-Range Weather Forecasting (ECMWF) (https://apps.ecmwf.int/datasets/), with a horizontal resolution of 0.75° × 0.75°.

Sea surface temperature data are derived from the Monthly Expansion and Reconstruction of Sea Surface Temperature (ERSST) with a 2° × 2° horizontal resolution provided by the National Oceanic and Atmospheric Administration of the United States (NOAA). The research period is from 1961 to 2015.

Data for the central intensities and locations of typhoons were obtained from the China Meteorological Administration Tropical Cyclone Optimal Path Database (tcdata.typhoon.org.cn). This database provides the Northwest Pacific Ocean's (including the areas of South China Sea, north of the equator and west of 180° E) typhoon routes since 1961 (Ying et al., 2014).

The Western Pacific Subtropical High Ridge Position Index employed in the following analyses was obtained from 74 circulation parameters provided by China Meterological Administration (https://cmdp.ncc-cma.net/cn/download.htm). The copyright belongs to the China Climate Diagnostics and Prediction Division of the National Climate Center. In addition, the monthly Pacific Decadal Oscillation index from 1961 to 2015 was obtained from the University of Washington (http://jisao.washington.edu/pdo/PDO.latest).

2.2 Methods

2.2.1 Criteria for an objective classification of major impacted large-scale circulations corresponding to extreme precipitation events

To explore the linkage between extreme precipitation and large-scale circulations, objective classification indicators are needed to categorize major impact large scale circulations corresponding to extreme precipitation events. The objective classification criteria of major impacted large-scale circulations and corresponding extreme precipitation events were specified prior to the start of the study as follows:

Step 1. Based on the China Meteorological Administration tropical cyclone database, we calculated the minimum distance (Dmin) from stations to the typhoon centers. To partition the typhoon precipitation, an accredited method named 'the objective technique for partitioning tropical cyclone precipitation' (Ren et al., 2007) is introduced. Typhoon precipitation is determined according to the relationship between the distance from each station to the center of typhoon. Critically, this method defines two important parameters: the absolute typhoon precipitation control distance (D0) and the possible typhoon precipitation control distance (D1) based on the radius of the typhoon peripheral flow system. The specific parameter setting is concretely shown in Table 1.

To ensure the maximum removal of typhoon precipitation interference for other types of precipitation, all the precipitation stations within D1 are considered as the precipitation stations impacted by *typhoon systems*, and the precipitation observed at these stations is defined as *typhoon precipitation*.

Step 2. For precipitation due to westerly systems, we made an objective division with the help of the westerly jet definition. The precipitation stations located north of the 200-hPa jet axis or the 200-hPa 25 m/s wind speed zone are considered as being mainly influenced by *westerly systems*, and the precipitation observed by these stations is defined as *westerly precipitation*. Scholars have highlighted that Xinjiang Province, which accounts for approximately one-sixth of China's land area, is not directly affected by the monsoon system in terms of climate (Yang et al., 2009). Therefore, the precipitation in Xinjiang Province is classified as *westerly precipitation* as well.

Step 3. After dividing *typhoon systems* and *westerly systems*, the rest of precipitation is modulated by both *westerly systems and subtropical systems*. We define this remaining precipitation as *westerly subtropical precipitation*.

2.2.2 Wave activity flux

In this study, a three-dimensional wave activity flux is used to describe the energy propagation characteristics of wave trains. The wave activity flux is irrelevant to the wave phase with the WKB assumption, but its direction is consistent with the local group velocity of the stationary Rossby wave train, which could may reflect the dispersion direction of wave energy (Takaya and Nakamura, 2001). In the logarithmic pressure coordinate system, the horizontal and vertical components of the three-dimensional wave activity flux (W) can be expressed as:

$$W = \frac{P}{2000|U|}\begin{cases} u\left(v'^2 - \Psi' v'_x\right) + v(-u'v' + \Psi' u'_x) \\ u\left(-u'v' + \Psi' u'_x\right) + v\left(u'^2 + \Psi' u'_y\right) \\ \frac{f_0 R_0}{N^2 H_0}\left[u\left(v'T' - \Psi' T'_x\right) + v(-u'T' - \Psi' T'_y)\right] \end{cases} \quad (2.2.2)$$

P is atmospheric pressure; $U = (u,v)$ represents the basic flow field; $U' = (u',v')$ represents disturbed quasi-geostrophic wind; Ψ' is the quasi-geostrophic perturbation flow function; f_0 is a geo-strophic parameter; R_0 is the dry gas constant; H_0 represnts elevation; N^2 is the buoyancy frequency; and T is temperature.

2.3 Model

The model used in the study is the Community Atmosphere Model Version 5.1 (CAM 5.1) developed by the National Center for Atmospheric Research (NCAR). CAM5.1 is a relatively new numerical model system for atmospheric research that improves upon CAM 3, especially for the dynamic frame as well as with physical and chemical processes (Neale et al., 2010). To verify our conclusions drawn from the observational and reanalysis data, this study utilizes CAM 5.1 to capture the large-scale circulation anomalies after the sea surface temperature forcing, which may be the possible forcing sources impacting northern China late summer extreme precipitation. The experiments are divided into a control run and sensitivity run. The latitude-longitude grid spacing is 1.9° × 2.5°. With the top layer at 3.6 hPa and the bottom layer at 992 hPa, the vertical direction has 30 layers. An significant important feature of the model is the time integration, which is set at up to 15 years.

3. Results for extreme precipitation in northern China

3.1 Classification and spatial-temporal distributions of extreme precipitation

Northern China is vast in territory and differs greatly in precipitation conditions between its western (dry) and eastern (wet) parts. Thus, precipitation indices that thoroughly describe the characteristics of extreme precipitation in northern China are undoubtedly critical. Presently, several categories of extreme precipitation indices recommended by the Climate Variability and Predictability Expert Team on Climate Change Detection and Indices are widely used, containing R10mm (Number of days with daily precipitation greater than 10 mm), CWD (Maximum number of consecutive wet days) and so on (Dulière et al., 2011). For precipitation situation of northern China, we selected the index of R10mm to represent the number of heavy precipitation days, and then we defined a new indicator ‘R10days’ to represent the extreme precipitation in northern China. In this study, R10days means the days when daily precipitation is greater than 10 mm, but not the count, and this is its primary difference from the R10mm index.

As part of an area impacted by monsoons, northern China has its own special summer rainy seasons. This rainy season is usually from late July until the end of August. Therefore, this study focuses on the extreme precipitation from July 21st to August 31st and herein referred to as the “late summer” period.

Figure 1 shows the late summer averaged frequency of R10mm (a), the late summer averaged amount of precipitation in R10days (b) and the percent of R10days and total precipitation days in northern China from 1961 to 2015 (c). The average distribution of extreme precipitation in northern China appears to have both longitudinal and latitudinal diminishing trends. For the extreme precipitation days, the amount of extreme precipitation and the proportion of extreme precipitation, there are prominent regional differences. Therefore, the extreme precipitation events in northern China must be analyzed subregionally.

The combined actions of rugged topography, complex circulation backgrounds and diversiform water transport routes results in diverse regional characteristics for extreme precipitation in the different areas of northern China. To obtain the spatial and temporal distributions of extreme precipitation and provide references for regionalization, the first 6 EOF modes of R10mm during late summer explaining 42.8% of the total variance were performed, and the first three modes are shown in Figure 2. The first EOF mode represents the two levels of R10mm distributions. Combined with the continuous rising trend of PC1, the area north of 35° N in the central and eastern parts of northern China, corresponding to the Yellow River Basin, demonstrates an obvious decreasing trend; the area south of 35° N corresponding to the Yangtze River Basin presents an increasing trend. According to the second and the third EOF modes, areas west of 116° E and areas east of 116° E are highlighted because of opposite spatial distributions. This means these two areas shall not be divided into one climate subregion.

Based upon the spatial distribution of the first three EOF modes, the late summer R10mm data in northern China are categorized into 5 subregions labeled A to E, as shown in Figure 3. The A subregion typifies the western part of Northwest China (WNWC), which mainly covers Xinjiang Province. The B subregion typifies the eastern part of Northwest China (ENWC). The C subregion typifies North and Northeast China (NC). The D subregion typifies the Central China (CC) and the E subregion typifies East China (EC). Moreover, the Tibetan Plateau has a vast area but relatively few stations, so daily precipitation data at those stations are relatively limited. Considering this situation, the Tibetan Plateau and its surroundings are not involved in this study.

However, the same subregion contains multifarious R10mm trends in accordance with all EOF modes. For example, the B subregion and the E subregion both possess nearly opposite R10mm trends in the EOF first mode and second mode. This phenomenon suggests that the total extreme precipitation in one area may be the sum of various kinds of extreme precipitation through multiple cooperating circulations. Therefore, it became increasingly necessary to objectively partition multiple circulations affecting extreme precipitation events and then investigate each of them individually.

To separate mixed circulations, the objective separation referred to in the Methods section is applied to extract three basic kinds of major impact circulations:

westerly, westerly subtropical and typhonic systems. Based upon these three major impact circulations, we in turn divide extreme precipitation events from the total R10mm in northern China into the westerly mode (WM), westerly subtropical mode (WSM) and typhonic mode (TYM). Figure 3 depicts each station's percentage of WM (a), WSM (b), TYM (c) and TR in northern China during late summer from 1961 to 2015. WM clearly shows a latitudinal diminishing tendency and is mainly distributed (50% or more in total land area) in the A, B and C subregions. WSM ascends from low to high latitudes and is mostly distributed in subtropical zones, especially the D and E subregions where WSM occupies approximately 70% of the land area. TYM is mostly distributed in coastal regions, and the E subregion has largest TYM distribution. This phenomenon demonstrates that the westerly and westerly subtropical R10mm both play an important role in extreme precipitation events in northern China during late summer, but WM contributes more at higher latitudes and WSM primarily influences lower latitudes.

Once the three categories of R10mm were classified, we selected the areas with the most prominent EOF eigenvalues in each subregion and obtained the relative regional average as the symbolic frequency distribution of R10mm, which is illustrated in detail in Figure 4. For the total R10mm, the A and E subregions initially appeared to show an increasing trend but then slightly declined after 2005. Wang and Li (2005) pointed out that summer extreme precipitation events in Northwest China and in East China both have increasing trends over time, which is consistent with our analysis; the B and C subregions both decreased. Concretely, the B subregion showed a fluctuating, but overall decreasing trend, and the C subregion revealed a decadal decreasing trend; the D subregion first decreased over time, then gradually increased and finally decreased after 2005. The WM in each subregion varies greatly; however, the common point is that a high frequency of WM (1.5 times above average) occurs from the 1980s to the early 2000s. For WSM occurrences, the A subregion appears to be fluctuant and is relatively few in number; in the B and C subregions, WSM first maintains high frequency before 1989; after 1989, it depicts gradual declining trend; in the D and E subregions, WSM first decreases in 1960s, then fluctuates and gradually increases until 2005. Finally it decreases again after 2005; for TYM, comparatively speaking, it is abundant and stable in the E subregion.

In summary, the frequency distributions of R10mm in each subregion show some commonalities in addition to specific local characteristics. The total R10mm in A and E subregions rises but declines in B and C subregions. Although the WM tendencies in each subregion are not the same, they remained at a high intensity from the 1980s to the early 2000s, and then declined after 2005 except for D subregion. Therefore, what causes WM in each subregion to show such variations is a question worthy of pondering. The regulation of the WSM frequency distribution is also obvious; it can be seen from the fitting lines that WSM values in the B and C subregions maintains high frequency before 1989. The WSM values in D and E subregions show similar trend, which both decreases in 1960s and after 2005. WSM in the same latitude zone possesses a similar distribution trend, and this regulation indicates that the north-south swing of large-scale circulations possibly plays a strong leading role in WSM values. WPSH, as the strongest subtropical system in summer in the Northern Hemisphere, dominates summer climate; we explore the possible role of WPSH in regulating WSM later in this study.

3.2 Large-scale circulations affecting extreme precipitation in northern China

Previous research has documented the effect of westerly wind fluctuations on summer precipitation in China (Yan et al., 2007) and pointed out that the interannual variation in westerly winds is the reason for the interannual variation in the water vapor field in Northwest China (Simmonds et al., 1999). However, the relationship between the summer Westerly Index and precipitation, and especially extreme precipitation, is not thorough. We thus must determine whether the decadal fluctuation of westerly winds results in a decadal trend of WM in northern China. The traditional Westerly Index is the mean of the global 500 hPa height field difference of two latitude zones, 35° N and 55° N. Considering that the Westerly Index at different longitudes may have different effects on extreme precipitation in northern China, we calculated the Westerly Index at each longitude and carried out a correlation analysis with WM in northern China as shown in Figure 5. Figure 5(a) indicates that the key area of westerly winds acting on extreme precipitation is mainly located in Asia, and extreme precipitation in northern China is impacted by westerly wind fluctuation at 2 key areas; one is close to 90° E, the other is near 120° E. Therefore, according to the significance test at the 0.01 level, WM in the A subregion is controlled mostly by the westerly wind from 60° E to 120° E; WM in the C subregion is affected mostly by the westerly wind from 85° E to 115° E; WM in the E subregion is influenced mostly by the westerly wind from 110° E to 135° E. In spite of not passing the significance test at the 0.01 level, on the basis of a significance test at the 0.05 level, the B and D subregions situated in north-central China easily receive the impact from both sides and were regulated correspondingly by westerly wind fluctuations from 81° E to 102° E and from 88° E to 115° E.

From this analysis, a set of regional Westerly Index shown in Figure 6(a) are obtained by averaging the Westerly Index from 60° E to 135° E. The annual and decadal variations in the Regional Westerly Index obviously coexist. The Regional Westerly Index rose from 1961 to 1977, then fell from 1975 to 2005 and rose again from 2005 to 2015. There was also a turning year in the 1980s; before 1980, the Regional Westerly Index dominated positively; beginning in the 1980s, especially after 1986, the Regional Westerly Index showed dominant trend of negative values in spite of several positive anomalies. These characteristics of the Regional Westerly Index possibly correspond to WM occurring at a high intensity and frequency from the 1980s to 2000s and its decline from 2005 to 2015.

Conversely, WSM in the same latitude zone tends to have a similar distribution trend that may be the result of a north-south swing of WPSH. To prove this idea, further study on the ridge position that represents the north-south location of WPSH is vital. The Western Pacific Subtropical High Ridge Position Index in Figure 6(b) provided by China Meterological Administration was employed for the analysis of the subtropical impact on extreme precipitation From Figure 6(b), the Western Pacific Subtropical High Ridge Position Index has both annual and decadal features as well. The mid-1980s could represent a turning point that separates two different changing laws. A decreasing trend occurred from 1961 to 1988 and an ascending trend is seen after 1988.

To determine the relationship between all categories of large-scale circulations corresponding to extreme precipitation events in northern China, two sets of tables for the correlation analysis between the Regional Westerly Index, the Western Pacific Subtropical High Ridge Position Index and classified R10mm in each subregion are shown below. From Table 2, the TR values in the A, B, D and E subregions all have a close relationship with the Regional Westerly Index, with all passing the significance test at the 0.10 level and some even at the 0.01 level. WM in all subregions trends consistently negative with the Regional Westerly Index. This phenomenon indicates that westerly winds regulate extreme precipitation in northern China; when the Regional Westerly Index becomes stronger, the corresponding westerly wind grows strong, which is not favorable to WM in northern China; conversely, when the Regional Westerly Index becomes weak and its meridionality strengthens, the corresponding westerly wind declines but may assist WM in northern China.

The WSM in northern China shows multiple significant correlations with the Regional Westerly Index. WSM values in B and C correlate positively, but in D and E, WSM correlates negatively with the index. Opposite correlations between the WM, WSM in C and Regional Westerly Index make the correlation between TR values in the C subregion insignificant. When combined with Table 3, not only did westerly winds control the WSM in B, C, D and E but also the position of Western Pacific Subtropical High ridge greatly impacted the WSM. Similar to the relationship between WSM and Regional Westerly Index, while the WSM in B and C correlates with Western Pacific Subtropical High Ridge Position Index positively, the WSM in D and E correlates with this index negatively. This situation demonstrates that different configurations of westerly wind variations and the swing of the Western Pacific Subtropical High ridge favors WSM in different parts of northern China. When the westerly wind strengthens and the subtropical high elevates northward, the WSM in B and C starts increasing; when the westerly wind weakens and the subtropical high retreats southward, the WSM in D and E becomes stronger. From a numerical point of view, the correlation between the Regional Westerly Index and the WSM in C is lower than the correlation between the Western Pacific Subtropical High Ridge Index and WSM in the same area, thus indicating WSM in C has a closer relationship with the subtropical high. Similarly, the WSM in B seems to be closer to the westerly wind.

To further determine the role that the westerly wind anomaly and subtropical high anomaly play in late summer extreme precipitation in northern China, the multiple linear regression is employed to study the relationship between the Regional Westerly Index, Western Pacific Subtropical High Ridge Position Index and 500-hPa geopotential height field, as is shown in Figure 7. The effects of the westerly winds and WPSH on the 500-hPa geopotential height field contain both similarities and differences. In Figure 7(a), the regressed 500-hPa geopotential height field exhibits three clear significantly positive centers over the northeast Atlantic, near the Caspian Sea, and over the Yellow Sea of China; the three strongest negative centers are over the Eastern Pacific, northern Atlantic and a zone from the western coast of Europe to the Okhotsk Sea. Such a distribution pattern reveals a mid-high latitude wave-train beginning from the Greenland passes through Eurasia and eventually reaches the Yellow Sea of China, which is the representation of the PJ teleconnection wave pattern in East Asia. Due to the combined action of the positive centers near the Caspian Sea, over the Yellow Sea of China and the negative zone over Eurasia, the westerly wind between 35° N and 55° N strengthens. When the Regional Westerly Index is negative, the centers reverse and the westerly wind in northern China will go become weak, but the meridionality strengthens, which may be the embodiment of quasi-resonant anomalies of planetary waves (Petoukhov et al., 2016).

In Figure 7(b), while the 500-hPa geopotential height regression field differs considerably from its counterpart in Figure 7(a), including the centers over the Greenland, northeast Atlantic, the Eurasia and so on, their similarities lie in East Asia; this is because the negative centers are situated in northeast Asia and southeast Asia, with a strong positive center from the Yellow Sea of China to the east of Japan. This distribution pattern indicates that the relationship between the two sets of indices and the 500-hPa geopotential height is opposite in most cases; however, in east Asia, their correlations with the height field becomes consistent. This situation means that the positive and negative variations in the two indices symbolize two phases of the PJ teleconnection wave pattern. When the indices are both positive and negative at the same time, the PJ teleconnection wave pattern from Northeast Asia to Southeast Asia will be stronger. With the negative phase of the PJ teleconnection wave pattern, the negative center at the 500-hPa geopotential height field is located in the north part of northern China, leading to an enhanced WSM in the D and E subregions; conversely, when the phase of the PJ teleconnection wave pattern turns positive, the centers of 500-hPa the geopotential height field are opposite to the negative phase, thus favoring WSM in the B and C subregions. On the other hand, from the perspective of the distribution of multiple linear regression coefficients, the westerly systems may have greater roles under the synergistic action of westerly and subtropical systems.

According to previous analyses, WM shows a highly negative correlation with the Regional Westerly Index. However, we must still address why the systems represented by one set of the Regional Westerly Index show different distribution frequencies of WM in each subregion (see Figure 4). In other words, with the relatively large meridionality, we must determine the reasons for the subregional differences in WM in northern China.

To answer this question and explore the mechanism of westerly large-scale circulations affecting WM in northern China, the regression of the 500-hPa geopotential height for WM is shown in Figure 8. The figure shows that westerly systems affecting WM in each subregion of northern China are consistent with the opposite side of systems regressed by the Regional Westerly Index shown in Figure 7(a), including the negative center at the west coast of the North Atlantic and the latitudinal positive-negative-positive centers in east Asia forming a positive phase of the PJ teleconnection wave pattern. WM in northern China, except for the D subregion, is directly affected by the location of the PJ teleconnection wave pattern, which is significantly impacted by the negative center at the west coast of the North Atlantic. First, when the negative center at the west coast of the North Atlantic extends westward (Figure 8a), the positive phase of the PJ teleconnection wave pattern will also move westward, strengthening the troughs between the Caspian Sea and A subregion, which favors WM in A. Then, when this negative center is mainly stationed between the west coast of the North Atlantic and the Caspian Sea (Figure 8b, 8d), the PJ teleconnection wave pattern moves eastward. At this moment, the positive center over Eurasia is increasingly noticeable; when the zonal width of the positive center over Eurasia is relatively narrow, the negative center of the PJ teleconnection wave pattern covers B subregion, thus favoring WM in this area; when the zonal width of the positive center over Eurasia is wide, the negative center of the PJ teleconnection wave pattern moves southward, leading to stimulating conditions of WM in the D subregion. At last, when the negative center at the west coast of the North Atlantic extends further eastward and reaches the eastern Aral Sea (Figure. 8(c), 8(e)), the PJ teleconnection wave pattern correspondingly moves further eastward at the same time, and the negative center is situated from the Yellow River Basin to Japan. Similar to the second situation, the zonal width of the positive center over Eurasia determines the zones prone to WM; the narrow zonal width of the positive center over Eurasia results in the C subregion being prone to WM, and the wide zonal width of the positive center over Eurasia leads to the E subregion being prone to WM. Accordingly, during the summer of 2010, a record-breaking heat wave occurred over eastern Europe and a large-scale flood occurred in the Yangtze River Basin of China, which was possibly caused by the PJ teleconnection wave pattern.

Similar to the above analysis, to understand the mechanisms and explore the cooperation of westerly large-scale circulations and subtropical large-scale circulations affecting WSM in northern China, a regression of the 500-hPa geopotential height fields for WSM in four subregions except for A is shown in Figure 9. The figure depicts that the key systems affecting WSM in B and C differ widely, which affects WSM in D and E. The main key systems affecting WSM in B and C contain a positive center at the west coast of the North Atlantic and a negative phase of the PJ teleconnection wave pattern in east Asia, which indicates that when the positive center at the west coast of North Atlantic appears and the WPSH extends northward, the PJ teleconnection wave pattern turns out to be negative, thereby helping WSM easily occur in B and C. Conversely, the main key systems affecting WSM in B and C contain a negative center at the west coast of the North Atlantic and a positive phase of the PJ teleconnection wave pattern in east Asia, which indicates that when the westerly meridionality grows strong and the WPSH is southward, the PJ teleconnection wave pattern turns positive, leading to WSM easily occurring in D and E.

4 The forcing sources of large-scale circulations affecting extreme precipitation in northern China

Through the above analysis, we speculate that the quasi-resonant anomalies of planetary waves manifested as westerly meridionality anomalies and the subtropical high anomalies manifested as the ridge position anomalies contribute to the WM and WSM in northern China. However, what stimulates these two categories of large-scale circulation anomalies has been unclear until now. A previous study documented that the SSTA in North Atlantic could excite the downstream Rossby wave train to modulate the circulations over Eurasia (Wu et al., 2012), and SSTA in Pacific Ocean could change the circulation patterns in northern China via weakening the EASM (Qian et al., 2013). Thus, we wish to determine if there is a relationship between the SSTA and westerly wind meridionality anomalies, and subtropical high ridge position anomalies. To prove this conjecture, we carried out an EOF analysis of the August SST in the north Atlantic and north Pacific and obtained the PCs. According to the correlation, PC3 of the North Atlantic SST correlates with the Regional Westerly Index the closest, and the correlation coefficient is 0.42, passing the significance level at 0.01; PC2 of the North Pacific SST correlates with Western Pacific Subtropical High Ridge Position Index the most, and the correlation coefficient is 0.29, passing the significance level at 0.05. The following analyses focus on the third mode of the

North Atlantic SST EOF and the second mode of the North Pacific SST EOF.

According to the third mode of the North Atlantic SST EOF, which explains 9.3% of the total variance, a tripole SST pattern is obviously exhibited with a negative center near Greenland, a negative center below 30° N and two positive centers sandwiched between these 2 negative centers. The corresponding PC3 shows both annual and decadal variation trends. PC3 first rose rapidly in the 1960s and 1970s, then declined from 1980 to 2010; finally, PC3 rose again in the past ten years. The trend of PC3 is basically consistent with the Regional Westerly Index, which means that PC3 may impact westerly wind meridionality anomalies.

The second mode of the North Pacific SST EOF explains 18% of the total variance. The spatial distribution vividly demonstrates a two-level SST pattern, with a positive zone in the center of North Pacific and a negative zone at lower latitudes, which is the distribution of Pacific Decadal Oscillation (PDO) cold phase. In addition, for PC2 of the North Pacific SST EOF, the correlation coefficient between PC2 and the corresponding monthly PDO index is up to -0.90 (figure omission), and it shows an opposite trend in the early and late periods with 1985 as the demarcating point. The trend of PC2 is basically consistent with the Western Pacific Subtropical High Ridge Position Index, indicating that the PDO cold phase facilitates the northward uplift of the subtropical high. Ye et al. (2014) once pointed out that when the PDO turns into the cold phase, strong south wind located on the west of the WPSH could supply opportunities for northward shift of the WPSH; while, when the PDO phase becomes warm, the heating from cumulus convective condensation is against development of the south wind, leading to the little opportunity for the WPSH to move northward and this is consistent with our study.

Since China is far from the North Atlantic geographically, we sought to determine how the SSTA of the North Atlantic influences the westerly wind variation between 60° E and 135° E and affects extreme precipitation in northern China. Prior studies have pointed that the transfer of wave activity plays a large part in the genesis of downstream cyclone systems (Trigo et al., 1999). To evaluate the wave energy stimulated by SSTA in the North Atlantic, we regressed the 500-hPa horizontal T-N wave flux to the PC3 of the North Atlantic SST and exhibited its divergence of the 500 hPa horizontal T-N wave flux in Figure 11(a). In addition, we regressed the 500-hPa geopotential height field to PC3 in Figure 11(b) as well. PC3 of the North Atlantic SST is closely correlated with the 500-hPa horizontal T-N wave flux, especially for the flux between 50° E and 140° E, which is increasingly intensive and continuous. Based on the 500-hPa geopotential height field for PC3, the positive center between the Aral Sea and Lake Balkash and the positive center located at 110° E (red boxes) are the 500 hPa horizontal T-N wave flux convergence zones, which suggests that the horizontal T-N wave flux stimulated by the North Atlantic SST may be helpful in maintaining the anomalous ridges in these two areas. However, from the climatology point of view, the systems here are troughs. Thus, when the North Atlantic SSTA appears to be a latitudinal positive-negative-positive tripole pattern, the downstream systems in the areas marked by red boxes are anomalous ridges that may weaken climatological troughs and the meridionality in westerly wind, thereby decreasing extreme precipitation in northern China. This conclusion is consistent with former analyses.

To further verify the roles that the North Atlantic SSTA play, CAM 5.1 is employed to analyze the response of large-scale circulations over Eurasia to the sea surface temperature forcing sources. This experiment contained two parts, a 15-year control experiment (CTRL) and a 15-year SSTA experiment (E01). CTRL employed the original climatic sea surface temperature in model as the lower boundary condition and ran from January of the first year to December of the fifteenth year. E01 is for the North Atlantic SSTA ranging from 100° W to 40° E and from 10° N to 70° N according to the former analyses. The spatial distribution of the third EOF mode SST in the North Atlantic (see Figure 10) was taken as a hypothetical SSTA, and its magnitude was unified with the climatic sea surface temperature data; then, it was added to the August climatic SST field as the lower boundary conditions of the model. E01 ran for 15 years from January to December.

Figure 12 demonstrates the July August mean climatic large-scale circulation anomalies in 15 years captured by the model. It shows the large-scale circulation anomalies' response to the North Atlantic SSTA. A northwest-southeast wave train structure forms a a negative zone near Caspian Sea and a PJ teleconnection pattern with a negative zone over northern China. This means that when North Atlantic appears with a positive-negative-positive pattern SSTA, the meridionality will enhance with westerly winds, which results in a geopotential height reduction and deepening troughs in northern China that favor extreme precipitation. This modulation corresponds to our previous speculations.

5 Conclusion and summary

This study shows the late summer extreme precipitation events characterized by R10mm in northern China that have occurred from 1961 to 2015 with specific non-uniformity. In considering that non-uniform extreme precipitation is the result of various circulation configurations, this study establishes an objective classification of the major impacts of large-scale circulations corresponding to extreme precipitation events. Utilizing the circulation classification, this study divides extreme precipitation into westerly mode (WM), westerly subtropical mode (WSM) and typhoon mode (TYM), thereby carrying out individual evaluations of types of extreme precipitation in northern China.

During the late summer, WM in northern China shows decadal characteristics with high frequencies in 1980s, 1990s and 2000s, which is in response to the enhancement of meridionality in westerly winds. This enhancement may strengthen the latitudinal positive-negative-positive circulation distribution of Pacific-Japan Wave Train Patterns in East Asia, with a relatively lower geopotential height area in northern China that favors an ascending motion, which is the necessary condition of extreme precipitation. However, with the westerly wind meridionality enhancement, the anomalous low-pressure system at the east coast of the North Atlantic and the anomalous high pressure system over Eurasia are critical for WM in northern China. The location of the anomalous low pressure system at the east coast of the North Atlantic impacts the longitudinal position of subregions prone to WM, and the zonal width of the anomalous high pressure system over Eurasia affects the latitudinal position of subregions prone to WM, which may explain the difference among the frequency distributions of WM in each subregion of northern China.

Differing from WM, the late summer WSM in the eastern parts of Northwest China, North and Northeast China have frequency distributions with a declining trend, especially before 1990; moreover, the WSM frequencies in Central China and East China are more similar, as they experience a downward-stable-downward trend. Based upon these phenomena, this study finds that the enhancement (abatement) of the westerly wind meridionality and the relatively southward (northward) position of Western Pacific subtropical high (WPSH) leads to a stretching southward (northward) front rain belt on the northwest edge of WPSH, thereby favoring WSM in Central China and East China (the eastern parts of Northwest China, North and Northeast China) (see Figure 13).

This study also investigates the possible forcing sources influencing the decadal variations in meridionality in westerly winds and the Western Pacific subtropical high ridge positions, which are tripole sea surface temperature anomalies in the North

Atlantic and PDO, respectively. Latitudinal positive-negative-positive tripole sea surface temperature anomalies in the North Atlantic could stimulate the perturbation wave energy and make westerly winds stronger, thus abating the meridionality and extreme precipitation in northern China. In contrast, the opposite tripole sea surface temperature pattern is beneficial to extreme precipitation. On the other hand, the cold phase of PDO could be helpful to the northward shift of the ridge line of WPSH.

From a westerly wind meridionality perspective, not only the forcing sources from the North Atlantic could impact the meridionality, but also could the signals from boreal areas of the northern hemisphere do that. Wang et al. (2003) pointed out that when the Mongolian Low Pressure is strengthened, the westerly will be stronger and the water vapor convergence in northern China will be increased. Is the Mongolian Low Pressure related to the Arctic Oscillation or the loss of Arctic ice? The signals in high latitude should be considered in the evaluation and prediction of extreme events.

6 Acknowledgements

This research was jointly supported by the National Key R&D Program of China (Grant No. 2018YFC1507101), the National Natural Science Foundation of China for Key Program (Grant No. 41630426;41975083), and by the Qing Lan Project and the Priority Academic Program Development of the Jiangsu Higher Education Institutions (PAPD).

7 References

Bates GT, Hoerling MP, Kumar A. 2001. Central U.S. Springtime Precipitation Extremes: Teleconnections and Relationships with Sea Surface Temperature. *J. Clim.* **14**: 3751-3766.

Belleflamme A, Fettweis X, Erpicum M. 2015. Do global warming-induced circulation pattern changes affect temperature and precipitation over Europe during summer?. *Int. J. Climatol.* **35**: 1484-1499.

Chen DL. 2000. A monthly circulation climatology for Sweden and its application to a winter temperature case study. *Int. J. Climatol.* **20**: 1067-1076.

Chen Y, Zhai P. 2014a. Precursor Circulation Features for Persistent Extreme Precipitation in Central-Eastern China. *Weather Forecast.* **29**: 226-240.

Chen Y, Zhai P. 2014b. Two types of typical circulation pattern for persistent extreme precipitation in Central-Eastern China. *Q. J. R. Meteorol. Soc.* **140**: 1467-1478.

Chen Y, Zhai P. 2015. Mechanisms for concurrent low-latitude circulation anomalies responsible for persistent extreme precipitation in the Yangtze River Valley. *Clim. Dyn.* **47**: 1-18.

Cheng M, He H, Mao D, Qi Y, Cui Z, Zhou F. 2001. Study of 1998 heavy rainfall over the Yangtze River Basin using TRMM data. *Adv. Atmos. Sci.* **18**: 387-396.

Du H, Wu Z, Zong S, Meng X, Lei W. 2013. Assessing the characteristics of extreme precipitation over northeast China using the multifractal detrended fluctuation analysis. *J. Geophys. Res. Atmos.* **118**: 6165-6174.

Dulière Valérie, Zhang Y, Salathé Eric P. 2011. Extreme precipitation and temperature over the U.S. Pacific Northwest: a comparison between bbservations, reanalysis data, and regional models. *J. Clim*. **24**: 1950-1964.

Easterling DR, Meehl GA, Parmesan C, Changnon SA, Karl TR, Mearns LO. 2000. Climate Extremes: Observations, Modeling, and Impacts. *Sci.* **289**: 2068-2074.

Gao T, Wang HJ, Zhou T. 2017. Changes of extreme precipitation and nonlinear influence of climate variables over monsoon region in China. *Atmos. Res.* **197**:

379-389.

Greenough G, Mcgeehin M, Bernard SM, Trtanj J, Riad J, Engelberg D. 2001. The potential impacts of climate variability and change on health impacts of extreme weather events in the United States. *Environ. Health Perspect* **109**:191-198.

Huang Y, Wang H, Fan K, Gao Y. 2015. The western Pacific subtropical high after the 1970s: westward or eastward shift?. *Clim. Dyn.* 44: 2035-2047.

Li J, Yu R, Zhou T. 2008. Teleconnection between NAO and Climate Downstream of the Tibetan Plateau. *J. Clim.* **21**: 4680-4690.

Kawamura R, Murakami T, Wang B. 1996. Tropical and midlatitude 45-day perturbations over the western Pacific during the northern summer. *J. Meteorol. Soc. Jpn.* **74**: 867-890.

Kim JS, Li CY, Zhou W. 2012. Effects of the Pacific-Japan teleconnection pattern on tropical cyclone activity and extreme precipitation events over the Korean peninsula. *J. Geophys. Res. Atmos.* **117**: 18109.

Li S, Shen B, Bo S, Huang B. 2017. The influences of East Asian Monsoon on summer precipitation in Northeast China. *Clim. Dyn.* **48**: 1647-1659.

Liu W, Wang L, Chen D, Tu K, Hu Z. 2015. Large-scale circulation classification and its links to observed precipitation in the eastern and central Tibetan Plateau. *Clim. Dyn.* **46**: 1-17.

Lu RY, Hong XW, Li XY. 2016. Asymmetric association of rainfall and atmospheric circulation over East Asia with anomalous rainfall in the tropical western North Pacific in summer. *Atmos. Ocean. Sci. Lett.* **9**: 1-15.

Mao J, Wu G. 2006. Intraseasonal variations of the Yangtze rainfall and its related atmospheric circulation features during the 1991 summer. *Clim. Dyn.* **27**: 815-830.

Meehl GA, Claudia T. 2004. More intense, more frequent, and longer lasting heat waves in the 21st century. *Sci.* **305**: 994-997.

Neale RB et al. 2010. Description of the NCAR Community Atmosphere Model (CAM5.0), Tech Rep NCAR/TN-486+STR. National Center for Atmospheric Research, Boulder, CO, USA.

Negri DH, Gollehon NR, Aillery MP. 2005. The Effects of Climatic Variability on US Irrigation Adoption. *Clim. Chang.* **69**: 299-323.

Ning L, Qian Y. 2009. Interdecadal Change in Extreme Precipitation over South China and Its Mechanism. *Adv. Atmos. Sci.* **26**: 109-118.

Nitta T. 1987. Convective activities in the tropical western Pacific and their impact on the Northern Hemisphere summer circulation. *J. Meteor. Soc. Japan* **65**: 373-390.

Orsolini YJ, Zhang L, Peters DHW, Fraedrich K. 2015. Extreme precipitation events over north China in August 2010 and their link to eastward-propagating wave-trains across Eurasia: observations and monthly forecasting. *Q. J. R. Meteorol. Soc.* **141**: 3097-3105.

Peng S, Robinson WA, Li S. 2003. Mechanisms for the NAO Responses to the North Atlantic SST Tripole. *J. Clim.* **16**: 1987-2004.

Petoukhov V, Petri S, Rahmstorf S, Coumou D, Kornhuber K, Schellnhuber HJ. 2016. Role of quasiresonant planetary wave dynamics in recent boreal spring-to-autumn extreme events. *Proc. Natl. Acad. Sci. U. S. A.* **113**: 6862-6867.

Qian C, Zhou T. 2013. Multidecadal Variability of North China Aridity and Its Relationship to PDO during 1900–2010. *J. Clim.* **27**: 1210-1222.

Qian W, Shi J. 2017. Tripole precipitation pattern and SST variations linked with extreme zonal activities of the western Pacific subtropical high. *Int. J. Climatol.* **37**: 3018–3035.

Ren F, Wang Y, Wang X, Li W. 2007. Estimating tropical cyclone precipitation from station observations. *Adv. Atmos. Sci.* **24**: 700-711.

Ren X, Yang XQ, Sun X. 2013. Zonal Oscillation of Western Pacific Subtropical High and Subseasonal SST Variations during Yangtze Persistent Heavy Rainfall Events. *J. Clim*. **26**: 8929-8946.

Simmonds I, Bi D, Hope P. 1999. Atmospheric Water Vapor Flux and Its Association with Rainfall over China in Summer. *J. Clim*. **12**: 1353-1367.

Song X, Song S, Sun W, Mu X, Wang S, Li J, Li Y. 2015. Recent changes in extreme precipitation and drought over the Songhua River Basin, China, during 1960-2013. *Atmos. Res.* **157**: 137-152.

Sun L, Ma L, Shen B, Dong W, Sui B. 2016. A diagnostic study of water vapor transport and budget of heavy rainfall over Northeast China during July to August 2010. *Chin. J. Atmos. Sci*. **40**: 630–646 (in Chinese).

Takaya K, Nakamura H. 2001. A formulation of a phase-independent wave-activity flux for stationary and migratory quasigeostrophic eddies on a zonally varying basic flow. *J. Atmos. Sci.* **58**: 608-627.

Tao SY, Chen LX. 1987. A review of recent research on the East Asian summer monsoon in China. In Monsoon Meteorology, Chang CP, Krishnamurti TN (eds). Oxford University Press: Oxford, UK, 60-92.

Trigo IF, Davies TD, Bigg GR. 1999. Objective Climatology of Cyclones in the Mediterranean Region. *J. Clim.* **12**: 1685-1696.

Van den Besselaar EJM, Klein Tank AMG, Buishand TA. 2013.Trends in European precipitation extremes over 1951-2010. *Int. J. Climatol.* **33**: 2682-2689.

Wang H. 2001. The Weakening of the Asian Monsoon Circulation after the End of 1970's. *Adv. Atmos. Sci.* **18**: 376-386.

Wang K, Cheng G, Xiao H, Jiang H. 2004. The westerly fluctuation and water vapor transport over the qilian-heihe valley. *Sci. Chin. Ser. D* **47**: 32-38.

Wang L, Qian Y, Zhang Y, Zhao C, Xiao C. 2016. Observed variability of summer precipitation pattern and extreme events in East China associated with variations of the East Asian summer monsoon. *Int. J. Climatol.* **36**: 2942-2957.

Wang Y, Li Z. 2005. Correction to "Observed trends in extreme precipitation events in China during 1961–2001 and the associated changes in large-scale circulation". *Geophys. Res. Lett.* **32**: L09707.

Wang Y, Zhou B, Qin D, Wu J, Gao R. Song L. 2017. Changes in Mean and Extreme Temperature and Precipitation over the Arid Region of Northwestern China:Observation and Projection. *Adv. Atmos. Sci.* **03**: 9-25.

Weng H, Wu G, Liu Y, Behera SK, Yamagata T. 2011. Anomalous summer climate in China influenced by the tropical Indo-Pacific Oceans. *Clim. Dyn.* **36**: 769-782.

Wu Z, Li J, Jiang Z, He J, Zhu X. 2012. Possible effects of the North Atlantic Oscillation on the strengthening relationship between the East Asian Summer monsoon and ENSO. *Int. J. Climatol.* **32**: 794-800.

Yan HS, Hu J, Fan K. 2007. The Analysis of Relationship between the Variation of Westerly Index in Summer and Precipitation during the Flood Period over China in the Last 50 Years. *Chin. J. Atmos. Sci.* **31**: 717-726 (in chinese).

Yang LM, Duolaite X, Zhang QY. 2009. Relationships between Rainfall Anomalies in Xinjiang Summer and Indian Rainfall. *Plateau Meteorol.* **28**: 564-572 (in Chinese).

Yang R, Xie Z, Jie C. 2017. A Dynamic Index for the Westward Ridge Point Variability of the Western Pacific Subtropical High during Summer. *J. Clim.* **30**: 3325-3341.

Yarnal B, Comrie AC, Frakes B, Brown DP. 2001. Developments and prospects in synoptic climatology. *Int. J. Climatol.* **21**: 1923-1950.

Ye T, Shen Q, Wang K, Zhang Z, Zhao J. 2015. Interdecadal change of the northward jump time of the western pacific subtropical high in association with the pacific decadal oscillation. *J.Meteor. Res.* **29**: 59-71.

Ying M, Zhang W, Yu H, Lu X, Feng J, Fan Y, Zhu Y, Chen D. 2014. An Overview of the China Meteorological Administration Tropical Cyclone Database. *J. Atmos. Ocean. Tech.* **31**: 287-301.

Yu R, Wang B, Zhou T. 2004. Troposphere cooling and summer monsoon weakening trend over East Asia. *Geophys. Res. Lett.* **31**: 217-244.

Yuan F, Chen W, Zhou W. 2012. Analysis of the role played by circulation in the persistent precipitation over South China in June 2010. *Adv. Atmos. Sci.* **29**: 769-781.

Zhang J, Chen H, Zhang Q. 2019. Extreme drought in the recent two decades in northern China resulting from Eurasian warming. *Clim. Dyn.* **52**: 2885-2902.

Zhang J, Tang Q, Chen H, Liu S. 2017. Northward shift in circulation system over the Asian mid-latitudes linked to an increasing heating anomaly over the northern Tibetan Plateau during the past two decades. *Int. J. Climatol.* **37**: 834-848.

Zhou TJ, Yu RC. 2005. Atmospheric water vapor transport associated with typical anomalous summer rainfall patterns in China. *J. Geophys. Res. Atmos.* **110**: D08104.

Zhu K, Xue M. 2016. Evaluation of WRF-based Convection-Permitting Multi-Physics Ensemble Forecasts over China for an Extreme Rainfall Event on 21 July 2012 in Beijing, *Adv. Atmos. Sci.* **33**: 1240-1258.

Table captions

Table 1 Parameter Setting of Objective Technique for Tropical Cyclone Precipitation

Table 2 Correlation coefficients between RWI and classified R10mm in regions

Table 3 Correlation coefficients between WPSHRPI and classified R10mm in regions

Figure captions

Figure 1 The average frequency of R10mm (a), the average amount of precipitation in R10days (b) and the percent of R10days and total precipitation days in northern China during late summer from 1961 to 2015 (c)

Figure 2 The first three EOF modes of R10mm in northern China during late summer and their corresponding normalized leading principal components (PCs). Units are arbitrary. The red lines in the right column are the fitting lines. The correlation coefficients between PCs and fitting lines all pass the significance test at the 0.10 level

Figure 3 Percentage distributions of the westerly mode (a), westerly subtropical mode (b) and typhonic mode in total R10mm precipitation during late summer in northern China and the zoning map of northern China

Figure 4 Frequency distribution of total R10mm (TR), westerly R10mm (WM), westerly subtropical R10mm (WSM) and typhoon R10mm (TYM) of each subregion; dotted lines represent mean values; red lines are the fitting lines; the values at the northwest corners are the correlation coefficients between indices and fitting lines; green stars represent the years which have high frequency of WM

Figure 5 Correlation coefficients between westerly R10mm (WM) in northern China(a), A subregion (b), B subregion (c), C subregion (d), D subregion (e), E subregion (f) and the longitudinal Westerly Index; the red lines represent a significance level of 0.10, and the blue lines represent a significance level of 0.01

Figure 6 Standardized Regional Westerly Index during late summer (a) and Standardized Western Pacific Subtropical High Ridge Position Index during July August (b); the dotted lines represent a zero value; red lines are the nine-point moving average; the values at the northwest corners are the correlation coefficients between indices and fitting lines

Figure 7 Multiple linear regression maps of 500-hPa geopotential height (units: gmp) regarding the Regional Westerly Index (a) and the Western Pacific Subtropical High Ridge Position Index (b); dotted areas indicate that the values are significant at the 90% confidence level as based on the F test

Figure 8 Regression maps of late summer 500-hPa geopotential height anomalies (units: gpm) regarding WM in A subregion (a), B subregion (b), C subregion (c), D subregion (d) and E subregion (e). Red boxes represent study areas. Dotted areas indicate that the values are significant at the 90% confidence level as based on the Student's t test

Figure 9 Regression maps of late summer 500-hPa geopotential height anomalies (units: gpm) for WSM in B subregion (a), C subregion (b), D subregion (c) and E subregion (d). Red boxes represent study areas. Dotted areas indicate that the values are significant at the 90% confidence level as based on the Student's t-test

Figure 10 The third EOF mode of the North Atlantic sea surface temperature anomalies and the second EOF mode of North Pacific sea surface temperature anomalies during August. Their corresponding normalized leading principal components (PCs) are in the right column. Units are arbitrary. The red lines in the right column are the Regional Westerly Index and Western Pacific Subtropical High Ridge Position Index

Figure 11 Regressed 500 hPa horizontal T-N wave flux for the PC3 of the North Atlantic SST and the correlation coefficients between their divergence (a); correlation coefficients between the 500-hPa geopotential height fields and the PC3 of the North Atlantic SST (b); black arrows and dotted areas represent the values passing the 90% confidence level. Red boxes represent key areas. Green lines respectively indicate climatological 5800 gpm and 5840 gpm

Figure 12 July August mean climatic 500-hPa geopotential height field anomalies during 15 years captured by the CAM 5.1 Model forced by SSTA in the North Atlantic

Figure 13 Sketch map of the effect of large-scale circulations on late summer extreme precipitation in northern China

Table 1 Parameter Setting of Objective Technique for Tropical Cyclone Precipitation

Maximum wind speed near the typhoon center/m s^{-1}		D0/km	D1/km
Long-range typhoon (Dmin≥300 km)	< 17.2 (tropical depression)	200	500
	17.2 ~ 24.4 (tropical storm)	300	700
	24.5 ~ 32.6 (severe tropical storm)	400	900
	≥32.6 (typhoon)	500	1100
Close-range typhoon (Dmin<300 km)	< 17.2 (tropical depression)	300	700
	≥ 17.2 (tropical storm, severe tropical storm and typhoon)	500	1100

Table 2 Correlation coefficients between RWI and classified R10mm in regions

Area	TR	WM	WSM	TYM
NWC	-0.45***	-0.50***	0.22	/
HRB	0.34**	-0.25*	0.53***	/
NC	-0.04	-0.40***	0.24*	0.01
CC	-0.51***	-0.40***	-0.47***	0.18
EC	-0.48***	-0.46***	-0.48***	0.08

*、**、*** respectively represent the correlation coefficients through 0.10, 0.05 and 0.01 significant levels

Table 3 Correlation coefficients between WPSHRPI and classified R10mm in regions

Area	TR	WSM	TYM
NWC	-0.18	-0.05	/
HRB	0.24*	0.30**	/
NC	0.16	0.29**	0.27**
CC	-0.31**	-0.25*	0.06
EC	-0.24*	-0.23*	0.16

*、**、*** respectively represent the correlation coefficients through 0.10, 0.05 and 0.01 significant levels

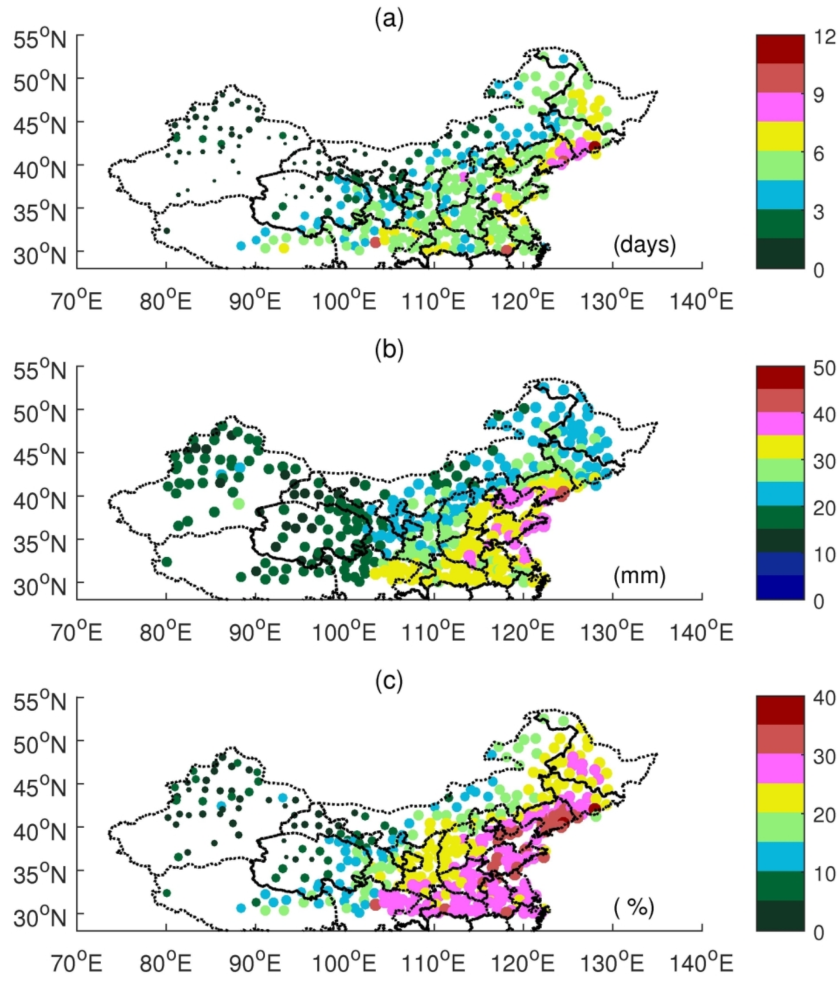
(a)
55°N
50°N
45°N
40°N
35°N
30°N
70°E
80°E
90°E
100°E
110°E
120°E
130°E
140°E
(days)
12
9
6
3
0
(b)
(mm)
50
40
30
20
10
0
(c)
(%)
40
30
20
10
0

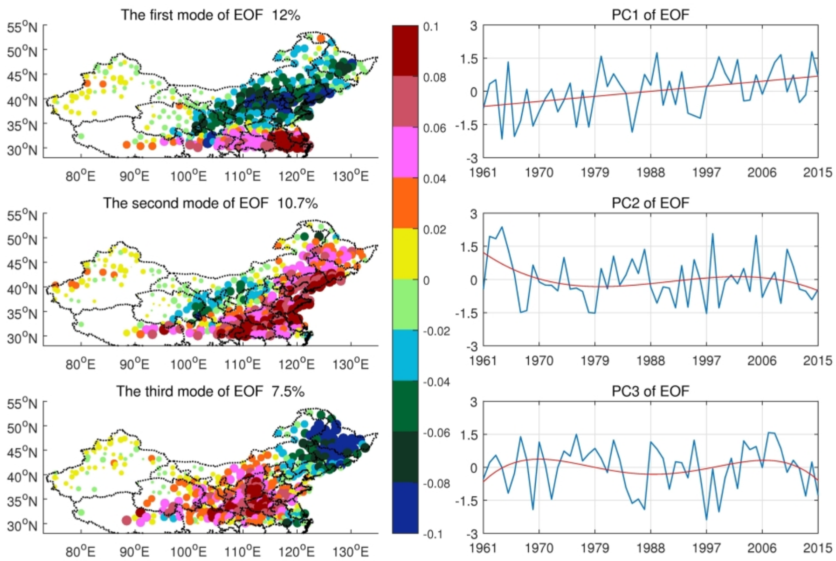
The first mode of EOF 12%
The second mode of EOF 10.7%
The third mode of EOF 7.5%
PC1 of EOF
PC2 of EOF
PC3 of EOF
55°N
50°N
45°N
40°N
35°N
30°N
80°E
90°E
100°E
110°E
120°E
130°E
0.1
0.08
0.06
0.04
0.02
0
-0.02
-0.04
-0.06
-0.08
-0.1
3
1.5
0
-1.5
-3
1961
1970
1979
1988
1997
2006
2015

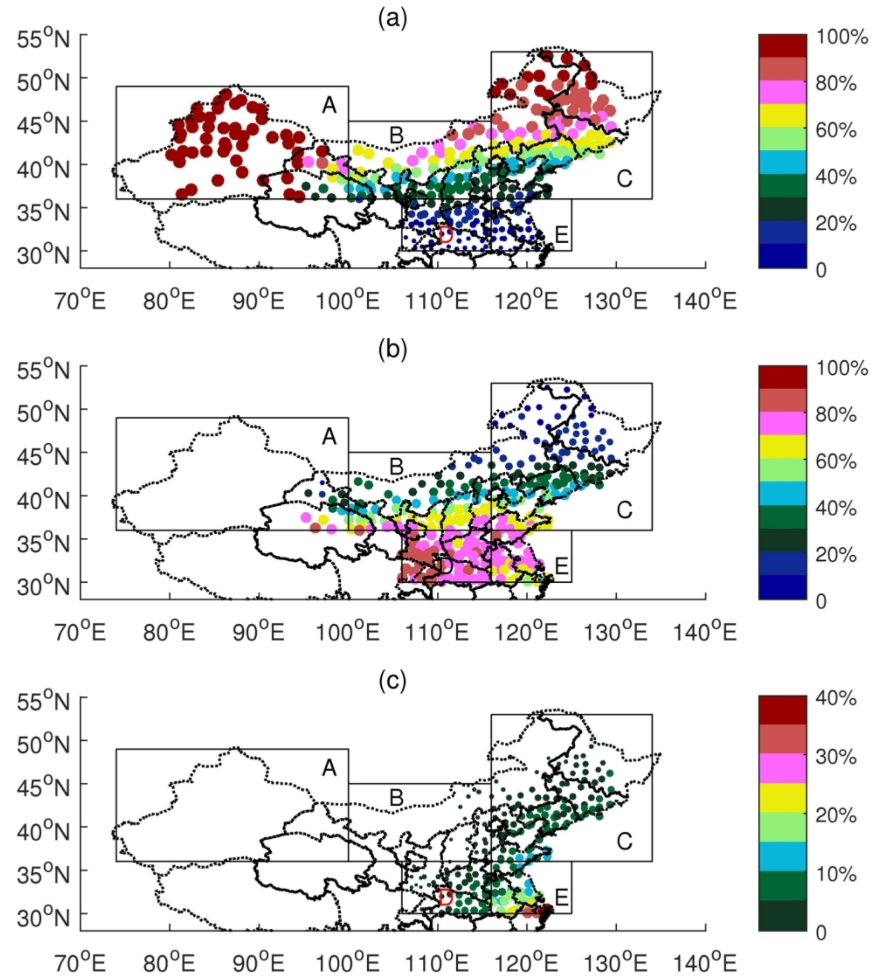

(a)
(b)
(c)
A
B
C
E
55°N
50°N
45°N
40°N
35°N
30°N
70°E
80°E
90°E
100°E
110°E
120°E
130°E
140°E
100%
80%
60%
40%
20%
0
40%
30%
20%
10%

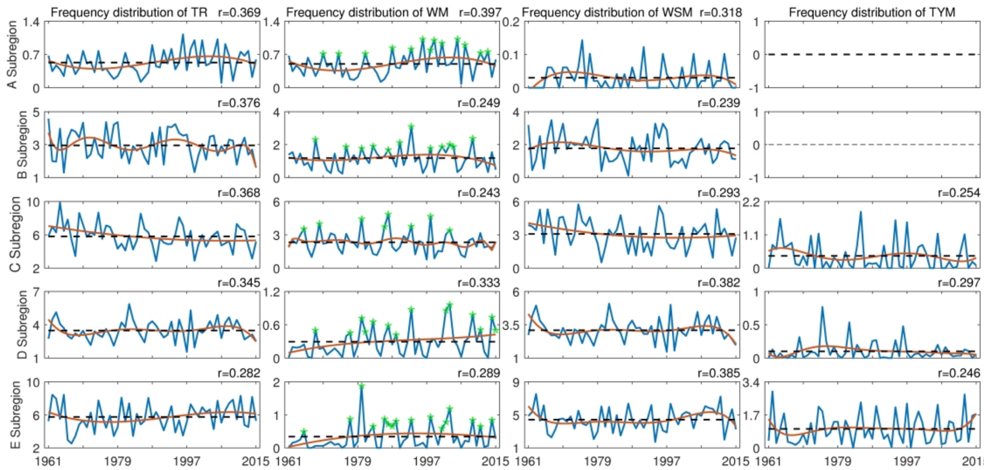
Frequency distribution of TR r=0.369
Frequency distribution of WM r=0.397
Frequency distribution of WSM r=0.318
Frequency distribution of TYM
A Subregion
B Subregion
C Subregion
D Subregion
E Subregion
r=0.376
r=0.249
r=0.239
r=0.368
r=0.243
r=0.293
r=0.254
r=0.345
r=0.333
r=0.382
r=0.297
r=0.282
r=0.289
r=0.385
r=0.246
1961
1979
1997
2015

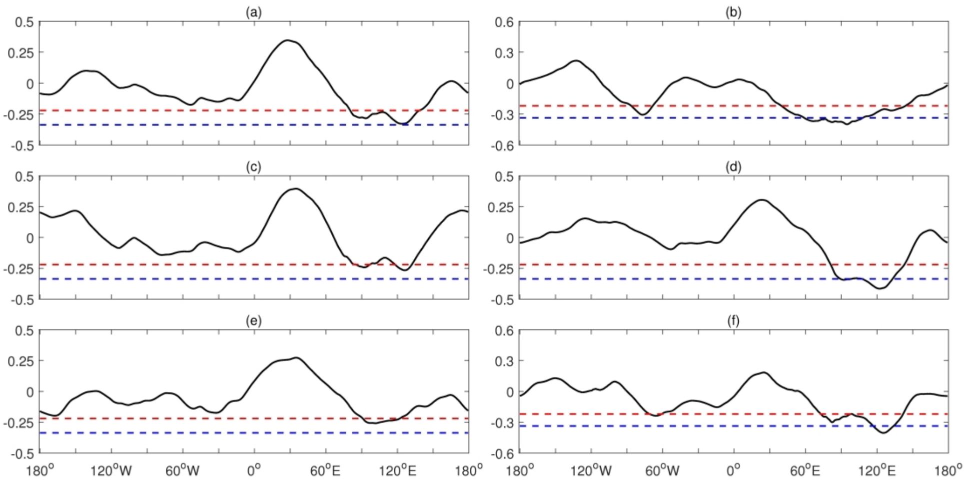

(a)
(b)
(c)
(d)
(e)
(f)
0.5
0.25
0
-0.25
-0.5
0.6
0.3
0
-0.3
-0.6
180°
120°W
60°W
0°
60°E
120°E
180°

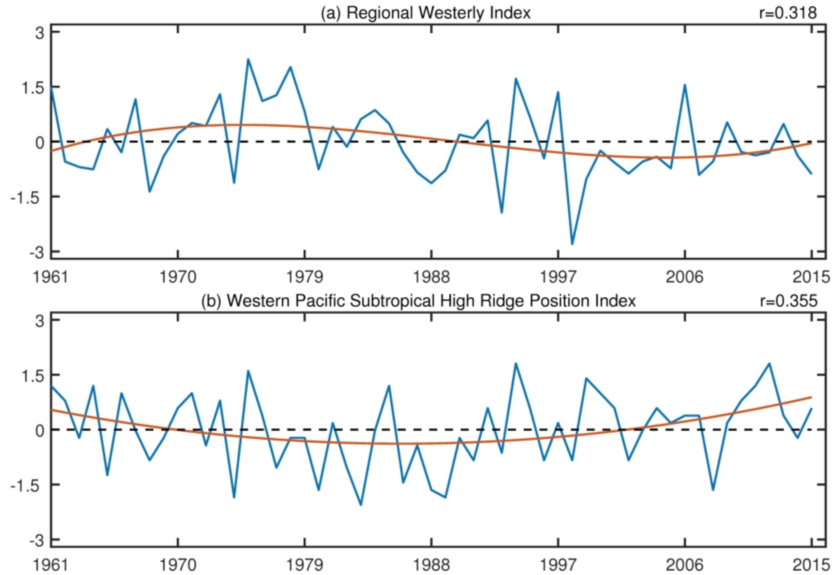
(a) Regional Westerly Index
r=0.318
3
1.5
0
-1.5
-3
1961
1970
1979
1988
1997
2006
2015
(b) Western Pacific Subtropical High Ridge Position Index
r=0.355
3
1.5
0
-1.5
-3
1961
1970
1979
1988
1997
2006
2015

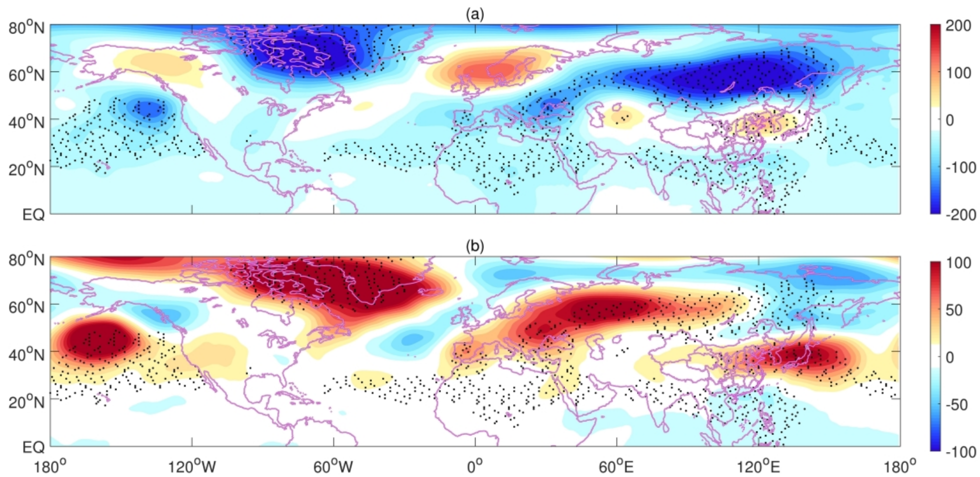

(a)
80°N
60°N
40°N
20°N
EQ
200
100
0
-100
-200
(b)
80°N
60°N
40°N
20°N
EQ
100
50
0
-50
-100
180°
120°W
60°W
0°
60°E
120°E
180°

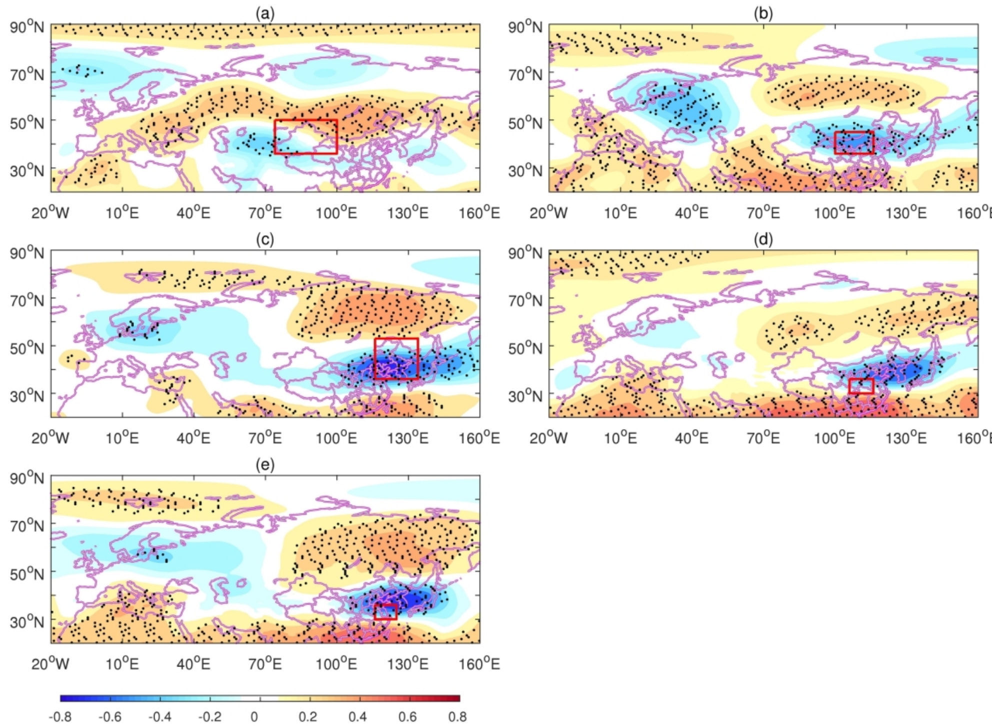
(a)
(b)
(c)
(d)
(e)
90°N
70°N
50°N
30°N
20°W
10°E
40°E
70°E
100°E
130°E
160°E
-0.8
-0.6
-0.4
-0.2
0
0.2
0.4
0.6
0.8

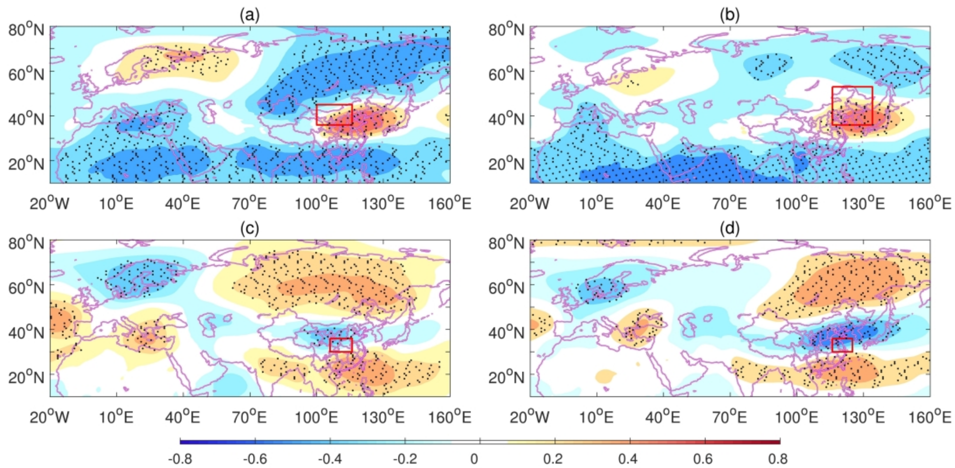
(a)
(b)
(c)
(d)
80°N
60°N
40°N
20°N
20°W
10°E
40°E
70°E
100°E
130°E
160°E
-0.8
-0.6
-0.4
-0.2
0
0.2
0.4
0.6
0.8

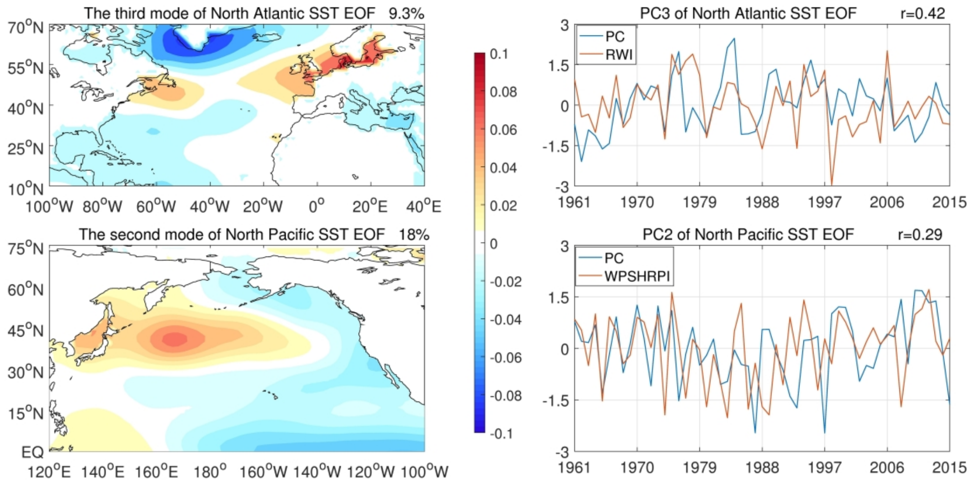
The third mode of North Atlantic SST EOF 9.3%
70°N
55°N
40°N
25°N
10°N
100°W 80°W 60°W 40°W 20°W 0° 20°E 40°E
The second mode of North Pacific SST EOF 18%
75°N
60°N
45°N
30°N
15°N
EQ
120°E 140°E 160°E 180° 160°W 140°W 120°W 100°W
0.1
0.08
0.06
0.04
0.02
0
-0.02
-0.04
-0.06
-0.08
-0.1
PC3 of North Atlantic SST EOF r=0.42
PC
RWI
3
1.5
0
-1.5
-3
1961 1970 1979 1988 1997 2006 2015
PC2 of North Pacific SST EOF r=0.29
PC
WPSHRPI
3
1.5
0
-1.5
-3
1961 1970 1979 1988 1997 2006 2015

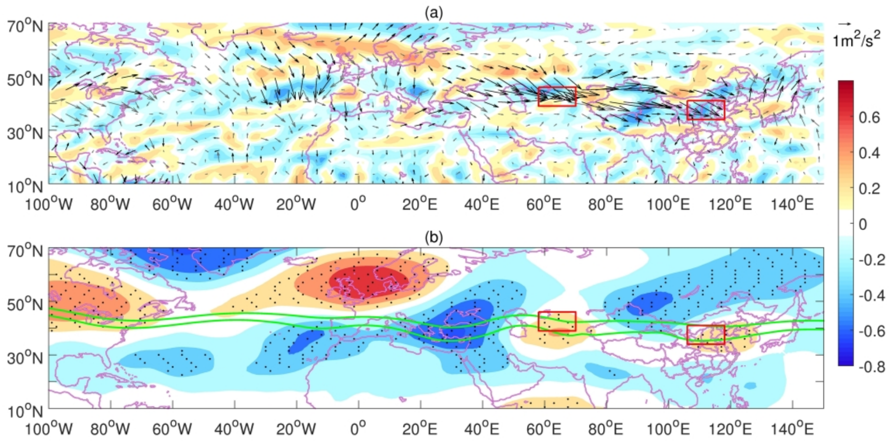
(a)
70°N
50°N
30°N
10°N
100°W 80°W 60°W 40°W 20°W 0° 20°E 40°E 60°E 80°E 100°E 120°E 140°E
1m²/s²
0.6
0.4
0.2
0
-0.2
-0.4
-0.6
-0.8
(b)
70°N
50°N
30°N
10°N
100°W 80°W 60°W 40°W 20°W 0° 20°E 40°E 60°E 80°E 100°E 120°E 140°E

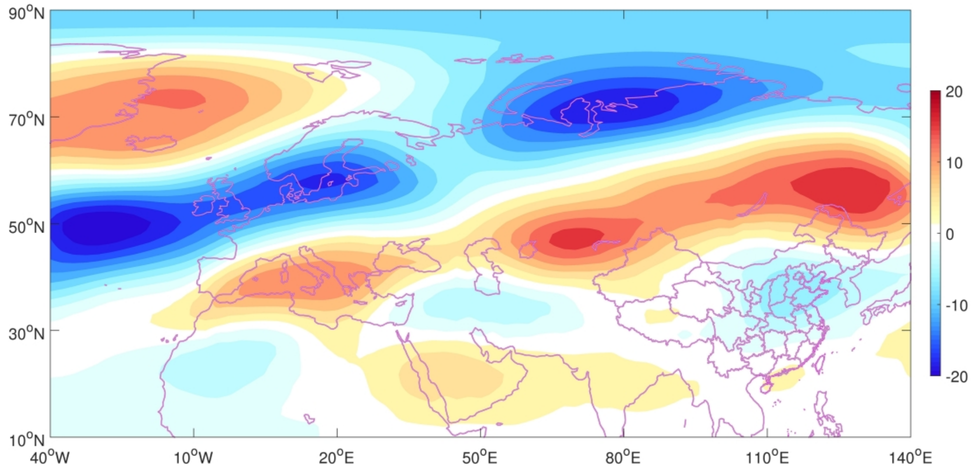
90°N
70°N
50°N
30°N
10°N
40°W
10°W
20°E
50°E
80°E
110°E
140°E
20
10
0
-10
-20

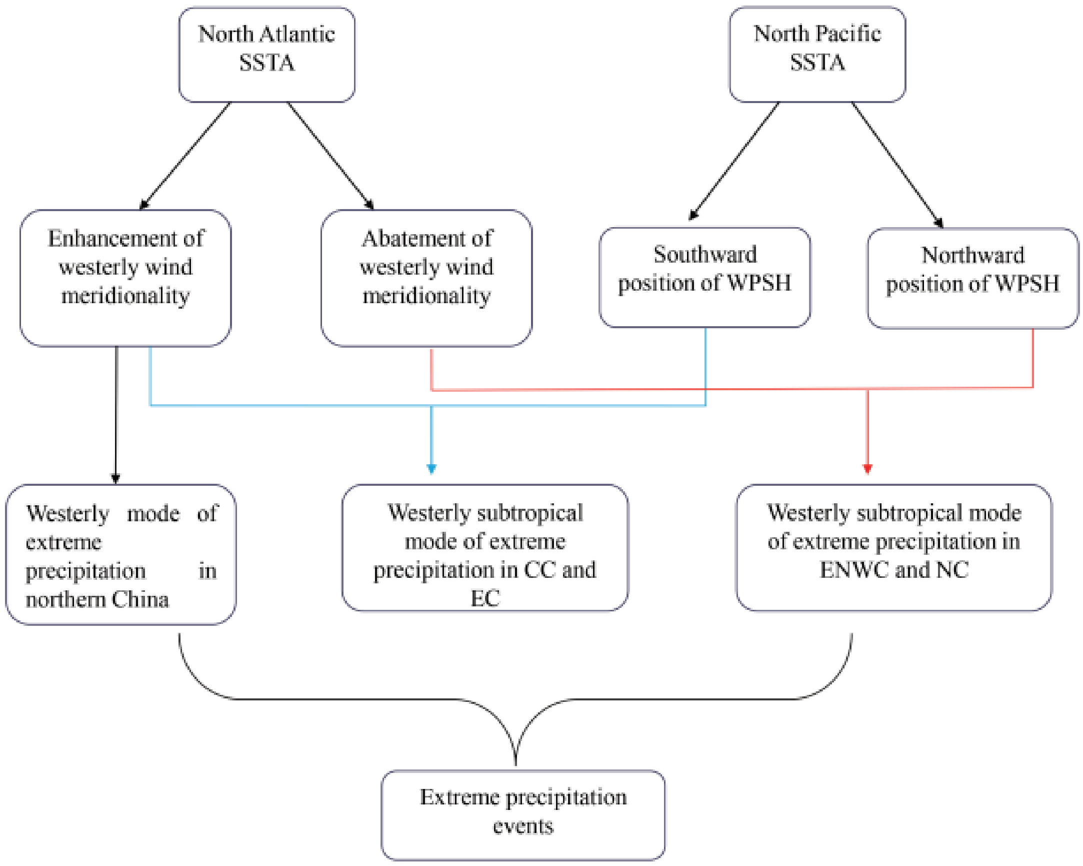
North Atlantic SSTA
North Pacific SSTA
Enhancement of westerly wind meridionality
Abatement of westerly wind meridionality
Southward position of WPSH
Northward position of WPSH
Westerly mode of extreme precipitation in northern China
Westerly subtropical mode of extreme precipitation in CC and EC
Westerly subtropical mode of extreme precipitation in ENWC and NC
Extreme precipitation events